



Experimental investigation and optimization of dimple-roughened impinging jet solar air collector using a novel AHP-MABAC approach

Mohammad Salman¹ · Ranchan Chauhan² · Tej Singh³ · Rajendran Prabakaran¹ · Sung Chul Kim¹

Received: 8 June 2022 / Accepted: 9 December 2022 / Published online: 22 December 2022
© The Author(s), under exclusive licence to Springer-Verlag GmbH Germany, part of Springer Nature 2022

Abstract

The effect of the flow and geometric parameters of a dimple-roughened absorber plate on the enactment of solar air collectors (SACs) with air-impinged jets was investigated in this study. The performance-defining criteria (PDCs) of a jet-impinged dimple-roughened SAC (JIDRSAC)-forced convection airflow system are significantly affected by variations in the system's control factors (CFs), such as the arc angle (α_{aa}) ranging from 30° to 75° , dimple pitch ratio (p_d/D_h) ranging from 0.269 to 1.08, and dimple height ratio (e_d/D_h) ranging from 0.016 to 0.0324. The constant parameters of the jet slot are a stream-wise pitch ratio (X_i/D_{hd}) is 1.079, a span-wise pitch ratio (Y_i/D_{hd}) is 1.619, and a jet diameter (D_i/D_{hd}) is 0.081. Based on the combined approach of the analytic hierarchy process and multi-attributive border approximation area comparison (AHP-MABAC), the Reynolds number (Re) = 15,000, $\alpha_{aa} = 60^\circ$, $p_d/D_h = 0.27$, and $e_d/D_h = 0.027$ depicted the best alternative (A-9) set among 16 alternatives to deliver the optimal performance of the JIDRSAC. The jet impingement pass compared to the smooth pass, the Nusselt number increased by 2.16–2.81, and friction factor increased by 3.35–5.95, and JIDRSAC was compared to the jet impingement pass, exhibiting an enhancement in Nusselt number and friction factor in the range of 0.55–0.80 and 0.05–0.15, respectively. In addition, sensitivity analysis is used to examine the ranking's stability and reliability in relation to the PDC weights.

Keywords Solar air collector · Air impinged · Dimple roughness · Optimization · AHP-MABAC · Exergetic efficiency

Abbreviations

| | |
|--------------|-------------------------------------------------------------|
| A_{ab} | Absorber plate surface area, m^2 |
| D_{hd} | The hydraulic diameter of the airflow duct, m |
| e_d | Indented dimple roughness depth, m |
| e_d/D_{hd} | Dimple height ratio |
| ff_i | Friction factor of jet impingement |
| ff_s | Friction factor of SPSAC |
| ff_{jd} | Friction factor of air with dimple roughness |
| h_{ct} | Convective heat transfer coefficient [$Wm^{-2}K^{-1}$] |
| H_d | Height of the duct, m |
| k_a | Thermal Conductivity of air, W/mK |
| L_d | Length of the duct, m |

| | |
|--------------|-------------------------------------------------------------|
| Nu_i | Nusselt number with jet impingement |
| Nu_s | Nusselt number of SPSAC |
| Nu_{jd} | Nusselt number with dimple roughness |
| p_d | Dimple roughness pitch, m |
| p_d/D_h | Relative indented dimple roughness pitch (dimensionless) |
| ΔP_d | The differential pressure across the length, Pa |
| Q_{uhg} | Useful heat gain to the working air, W |
| Re | Reynolds number |
| T_{abm} | Bulk mean temperature of the absorber plate, K |
| T_{ai} | Inlet air temperature, K |
| T_{ao} | Outlet air temperature, K |
| T_{am} | Mean temperature of the absorber plate, K |
| V_a | The velocity of flowing air, m/s |
| W_d | Width of the duct, m |
| SAC | Solar air collector |
| SPSAC | Single-pass solar air collector |
| JIDRSAC | Jet-impinged dimple-roughened solar air collector |

Responsible Editor: Philippe Garrigues.

✉ Sung Chul Kim
sungkim@ynu.ac.kr

¹ School of Mechanical Engineering, Yeungnam University,
280 Daehak-Ro, Gyeongsan-Si, Gyeongbuk 712-749, Korea

² Department of Mechanical Engineering, Dr B R Ambedkar
National Institute of Technology Jalandhar, Punjab 144011,
India

³ Faculty of Informatics, Savaria Institute of Technology,
ELTE EötvösLoránd University, Szombathely 9700, Hungary

Greek symbols

| | |
|---------------|-------------------------------------|
| ν | Kinematic viscosity of air, m^2/s |
| α_{aa} | Arc angle, ($^\circ$) |

| | |
|-------------|---------------------------------------|
| ρ_a | The density of air, kg/m ³ |
| η_{ex} | Exergetic Efficiency |

Introduction

As a consequence of industrial expansion and population growth, the rate of energy consumption increases. It causes economic distress as well as damage to the environment in the form of acid rain, global warming, ozone layer depletion, and many other phenomena (Perera 2017). Global CO₂ emissions from fossil fuels and trade have been essentially flat in recent years, owing to falling coal use globally as well as improved energy efficiency and increased use of renewable energy. The UN's Framework Convention on Climate Change (UNFCCC2015)'s Paris Agreement formally came into force in 2016. This agreement aims to check global warming temperatures to 1.5–2 °C overhead pre-industrial levels in the twenty-first century, and calls for the development of new technologies to manage CO₂ levels in the atmosphere (Arafa 2017). In a near-future energy scenario, technology transfer to 100% of renewable energy is being prioritized (Gielen et al. 2019). For the entire world, the COVID-19 lockdown has provided a vision of a clean air future (Landrigan et al. 2020). This has resulted in an increased understanding of renewable energy's ability to assist in the creation of clean, livable, and equal communities.

Employing renewable forms of energy, of which solar energy is by far the most popular, will help minimize energy demand from conventional, non-renewable sources. The modest and operative way to consume solar energy is to transform it into thermal energy for a variety of applications, including heating and electricity generation. The solar air collector (SAC), which is used for agricultural and industrial drying, building heating, and ventilation applications, is an appropriate technology for utilizing solar energy (Jain et al. 2021b). Because of the thermophysical characteristics of air and the formulation of the viscous sublayer, SAC has a low convective heat transfer rate (Azari et al. 2021). Detailed practical and theoretical studies conducted in the literature have enhanced the performance of SAC. Novel strategies to enhance the performance of SACs presented in the literature are discussed herein.

Sahu et al. (2021) revealed that the arc-shape rib roughened SAC has a maximum thermal efficiency of 71.6% for apex-upstream and 55.8% for apex-downstream than the smooth pass solar air collector (SPSAC) for a mass flow rate ranging from 0.010 to 0.047 kg s⁻¹. Kumar et al. (2021) analyzed the thermohydraulic performance of the SAC with zig-zag-shaped copper tubes and revealed that the maximum value of energy and exergy efficiency as 62.8% and 58.48% was obtained at an airflow rate of 0.05 kg/s. Tabish et al.

(2021) analytically evaluated the performance of the protrusion rib-roughened SAC and found that the net effective efficiency of 70.92% was achieved at a rib pitch ratio of 10 and rib height ratio of 0.0289. Kashyap et al. (2021) studied the consequences of a V-ribs with multiple gaps on the absorber plate of SAC with Reynolds number (Re) ranging from 2000 to 21,000. They revealed that due to the production of secondary-flow vortices on the absorber surface, the multiple V-ribs patterns with symmetric gaps resulted in a significant increase in Nusselt number (Nu) and a friction factor (ff). Rahmani et al. (2021) numerically simulated the performance of SAH with wavy and raccoon-shaped fins. They observed that increasing the fin height resulted in a 50% increase in Nu and ff escalation of nearly the same value. Hassan et al. (2021) investigated the thermal performance of multiple arc dimple-roughened SAC and found that the Nu increased by 2.87–5.61% compared to conventional SAC. Chauhan and Thakur (2014) studied the jet impingement SAC for Re ranging from 4000 to 16,000 and revealed that the thermohydraulic performance improves by 34.54–57.89% when compared to the conventional SAC. Chauhan and Kim (2019a, b) examined the thermohydraulic performance of an artificially roughened plate in an SAC, and concluded that the Nu and ff were both increased by 2.24 and 2.65, respectively. Furthermore, they investigated the effect of dimple roughening on effective efficiency and concluded that a pitch ratio of 10, a height ratio of 3, and a dimple arc angle of 60° resulted in an effective efficiency of 69.7%. Salman et al. (2021a, b) experimentally investigated the exergetic efficiency of an indented dimple-roughened absorber plate in a jet-impinged SAC. They revealed that at a temperature rise parameter of 0.03 km²/W, the maximum value of exergetic efficiency is 0.026. Goel et al. (2021) investigated the performance and parametric optimization of jet-finned SAC and found that the optimal values of the fin and jet slot parameters generated the maximum collector efficiency are 0.23 for the fin spacing ratio, 0.46 for the X_f/D_{hd} , and 0.076 for the D_f/D_{hd} .

Some authors have considered the heat transfer features of combined techniques utilized in single-pass SACs. Goel and Singh (2020b, a, 2022) experimentally compared the performance of a fin-type jet-impinged SAC and found that the thermal efficiency was 8% and 29% improved compared to the conventional and jet-impinged SAC, respectively. Moreover, fin-impinged SAC achieved a maximum enhancement in Nusselt number and effective efficiency of 2.45 and 82.5% at fin spacing ratio = 0.23 and X_f/D_{hd} = 0.46, respectively. Skullong et al. (2016, 2017) experimented with several artificial roughness configurations to enhance the thermal performance of SAC. It was found that the use of collective delta-wing and wavy-groove vortex creators enhanced the convective heat transfer rate. They concluded that for Re ranging from 4800 to 23,000, the thermohydraulic

performance of the combined SAC technique was augmented at approximately 37.7–46.3% higher than that of the grooved SAC. Furthermore, wavy grooves combined with a couple of trapezoidal winglets were utilized to enhance the thermohydraulic performance by 43% over the grooved individual SAC. Salman et al. (2021a, b) experimentally investigated the dimple-roughened absorber plate in jet-impinged SAC and determined that the optimal thermohydraulic performance value of 2.15 is attained at $Re = 15,000$ for roughness parameters, that is, arc angle = 60° , dimple pitch ratio = 0.269, and dimple height ratio = 0.0267. Goel and Singh (2021a) analytically investigated the performance of jet impinged SAC with fins attached to the absorber plate. They found that the maximum enhancement in temperature rise parameter and thermal efficiency of 20.5% and 16.4% at a D_f/D_{hd} of 0.076, respectively.

The purpose of all the preceding experimental studies was to investigate the features of heat transfer and frictional losses concerning specific use. The increase in heat transfer is attributed to a significant increase in frictional losses within the collector's duct, and both of these parameters are influenced by the geometric configuration and operational conditions. The heat transfer rate must be higher for a better system efficiency output, and the frictional losses are unpleasant and should therefore be taken into consideration. The goal of identifying the set of conditions under which the desired outcome occurs where the heat transfer is positioned at the highest level, while the undesirable frictional losses are placed at the lowest level, meets a study that arrays down the set of parameters that convey the maximum energy output of the energy conversion system and demonstrate its dominance. The collection of such a best parameter set necessitates a simple, systematic, and practical approach to guide researchers to consider several performance-defining factors and their interconnections.

A large number of test runs should be implemented in both numerical and experimental studies to determine the thermohydraulic performance of an SAC. The layout of the investigation methods can be used to reduce the number of test runs while also obtaining the thermophysical phenomena and optimum solutions. Multicriterion decision-making (MCDM) methods can be used to find solutions consisting of multiple alternatives and performance evaluation criteria that have gained widespread recognition for use in science, engineering, and management, among other fields (Chauhan et al. 2016; Jain et al. 2021a; Chauhan et al. 2017a, b; Yu et al. 2021; Abdul et al. 2022). An MCDM is a procedure that specifies how attribute data are analyzed to choose the best option among several alternatives. It includes a variety of procedures, such as gray relation analysis, preference ranking arrangement, compromise ranking approach, a method for enrichment evaluation order preference strategy based on resemblance to perfect clarifications, and a

successful analytic hierarchy process (AHP) that has been utilized to tackle a slew of decision-making issues. Although several MCDM methods exist in the literature to help designers find the best alternative, most of these methods are difficult to understand and use, requiring a high level of mathematical complexity. Among various MCDM methods (Wang et al. 2017; Rani and Tripathy 2022; Sharma et al. 2017; Singh et al. 2016; Chauhan et al. 2017a, b; Zhao et al. 2021; Abdollahpour et al. 2020), AHP and multi-attributive border approximation area comparison (MABAC) are the most widely utilized ones to address renewable and sustainable energy constraints (Heo et al. 2010; Kahraman et al. 2009). AHP has been utilized by researchers in a variety of situations, such as proposing a public work contract (Bertolini et al. 2006) and selecting a phase change material for thermal storage in solar air systems (Xu et al. 2017). The MABAC approach was employed by a majority of researchers for an assortment of applications, including the selection of hotels on business trip sites (Yu et al. 2017), guided anti-tank missile battery's defensive operation (Bojanic et al. 2018), and commercially available scooters (Biswas and Saha 2019). The advantage of the integrated AHP-MABAC approach is that it aids in the evaluation of optimal alternatives when there is a disagreement about the relative relevance of the criteria and requires fewer numerical calculations.

The key objective of this study was to determine whether the integrated AHP-MABAC approach can be used to predict the enactment of a jet-impinged SAC with a dimple-roughened absorber plate (JIDRSAC). To accomplish this objective, an investigation was directed to identify the heat transfer rate and frictional losses, which were used to evaluate the optimal constraints. To evaluate the effect of dimple roughness, the optimal set of jet plate parameters, that is, streamwise jet pitch ratio = 1.079, spanwise jet pitch ratio = 1.619, and circular jet diameter ratio = 0.081 were kept constant throughout the test. The purpose of this study was to evaluate the effect of airflow and dimple roughness parameters dimensionalized by the hydraulic diameter (D_h) of the duct, that is, the arc angle (α_{aa}) ranging from 30° to 75° , dimple pitch ratio (p_d/D_h) ranging from 0.269 to 1.08, and dimple height ratio (e_d/D_h) ranging from 0.016 to 0.0324 on the performance of JIDRSAC. The impact of dimple roughness parameters on the overall performance is also explored to reach an optimal geometrical arrangement that places the desired heat transfer at its highest level while minimizing frictional losses inside the JIDRSAC duct. The quantitative estimation of these parameters is relatively broad and increases the experimental cost and time. Therefore, the trials were designed using the AHP-MABAC, followed by the percentage contribution of the parametric effect over the performance measures. The exergetic efficiency (η_{ex}) performance of the system with respect to the

heat transfer rate and frictional losses was considered, and parameters affecting the performance, that is, Re , p_d , α_{aa} , and e_d , were also investigated. To the authors' best knowledge, the use of the AHP-MABAC on JIDRSAC has not been investigated before, and it is evident that the optimum set of parameters leads to the maximum η_{ex} of a SAC system.

Experimental setup

As showed in Fig. 1a, an experimental setup was prepared and implemented to investigate dimples on an absorber plate in a jet impingement SAC. It comprises a rectangular-shaped duct measuring 2000 mm × 250 mm × 25 mm, a supporting frame, a pyranometer (SR05-D1A3, Hukseflux), a solar flux simulator panel, a data acquisition panel (National Instruments), a plenum, an orifice meter (Samdukeng), and an air blower (dongkun-DB 301). Figure 1b depicts a schematic of the JIDRSAC duct shape and dimensions. The entry and exit lengths are considered as per the ASHRAE (ASHRAE standard 93 2003), $\geq 5\sqrt{W_d \times H_d}$ and $\geq 2.5\sqrt{W_d \times H_d}$, respectively. Table 1 lists the characteristics and dimensions of the components used. The flow rate of air was measured using a manometer connected through a Pitot tube in accordance with the guidelines of the International Committee for Measures and Weights (CIPM-81–91) (Picard et al. 2008). By using 50-mm-thick glass wool with thermal conductivity of $0.0343 \text{ Wm}^{-1} \text{ K}^{-1}$, the duct is well insulated from three sides to minimize heat loss to the environment. The SAC duct was planned sensibly so that the dimple-roughened absorber plate was fitted at its location. The gap maintained among the backplate, jet plate, dimple-roughened absorber plate, and top glass cover was using acrylic spacers. The absorber plate is made of aluminum with a thickness of 1 mm. Using a circular tip indenter tool, the dimple roughness geometry was manually created beneath the absorber plate (Bhushan and Singh 2011). The dimple-roughened absorber plate is illustrated in Fig. 1c.

On the top of the SAC duct, the 12 halogen lamps fixed to the iron frame are assembled in four rows with three in each row to produce a solar flux of 1000 W m^{-2} . Each halogen lamp was graded at 500 W and controlled by autotransformers and regulators. A digital solarimeter was coupled to the computer via a data logger to check the consistency of the solar flux along the test section. The temperatures of the inlet air, dimple-roughened heated plate, and outlet air were noted using a K-type thermocouples. A set of three thermocouples each at the entry and exit sections was arranged along the midway of the duct's height. Along the test section length, fifteen thermocouples were coupled with the absorber plate at different locations as

shown in Fig. 2a. The average value of the thermocouples was used to calculate the temperature along the duct. Figure 2b displays the air temperatures inside the duct and along the absorber plate. The absorber plate's temperature showed linear variation in the airflow direction. Temperature variations in the direction normal to the absorber plate could not be measured because of the narrow duct depth, thus they were assumed to be minimal. A difference in pressure along the test section's length was provided via two pressure taps at the entry and exit sections. The software LabVIEW was designed to store all of the data collected as experimental results in the workstation via a data logger. The range of airflow and dimple-roughened absorber plate parameters, namely p_d/D_h , α_{aa} , and e_d/D_h , for optimization are given in Table 2. These parameters must be optimized to produce a set of Re , p_d/D_h , α_{aa} , and e_d/D_h that predict the maximal convective heat transfer with a minimal frictional penalty inside the duct.

The scripts of Duffie and Beckman (2013) were used to acquire the thermo-physical properties of air, such as thermal conductivity (k_a), specific heat (C_p), kinematic viscosity (ν), and density (ρ_a). The obtained values of these important parameters were utilized to calculate the values of the fundamental procedure parameters, which were then used to evaluate the performance-defining criteria (PDCs). The procedure parameters, namely velocity of flowing air (V_a), hydraulic diameter (D_{hd}), Re , h_{cr} , Nu_{jd} , and f_{jd} were calculated as follows (Salman et al. 2021a, b):

V_a is considered with the assistance of the obtained mass flow rate (m_a) through the data logger as

$$V_a = \frac{m_a}{\rho_a W_d H_d} \quad (1)$$

where m_a is the mass flow rate of air.

The hydraulic diameter is evaluated as

$$D_{hd} = \frac{2(W_d \times H_d)}{(W_d + H_d)} \quad (2)$$

The Re of airflow in the SAC duct is intended from

$$Re = \frac{V_a \times D_{hd}}{\nu} \quad (3)$$

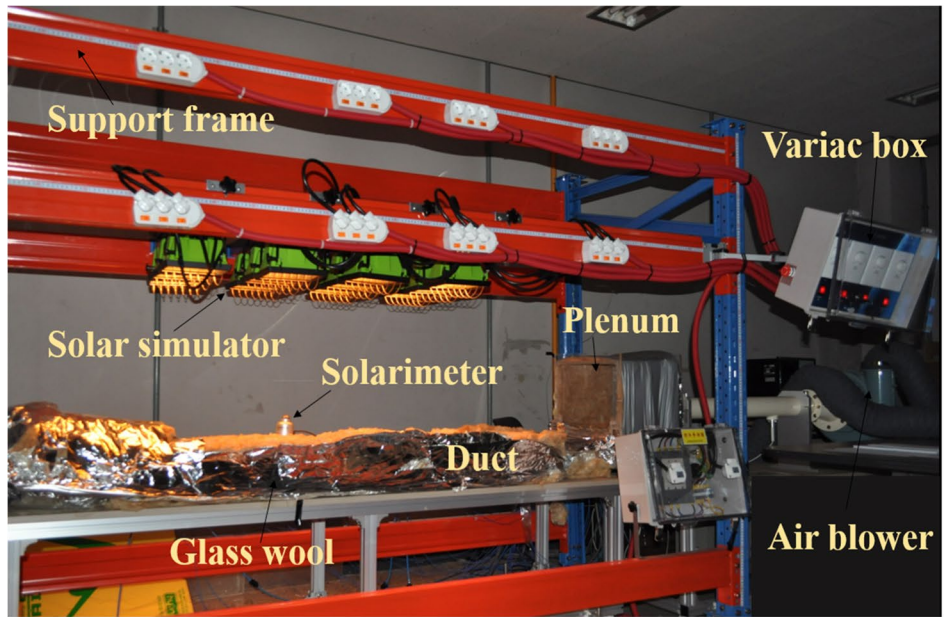
The useful heat gain (Q_{uhg}) is given by

$$Q_{uhg} = m_a C_p (T_{ao} - T_{ai}) = h_{ct} A_{ab} (T_{abm} - T_{am}) \quad (4)$$

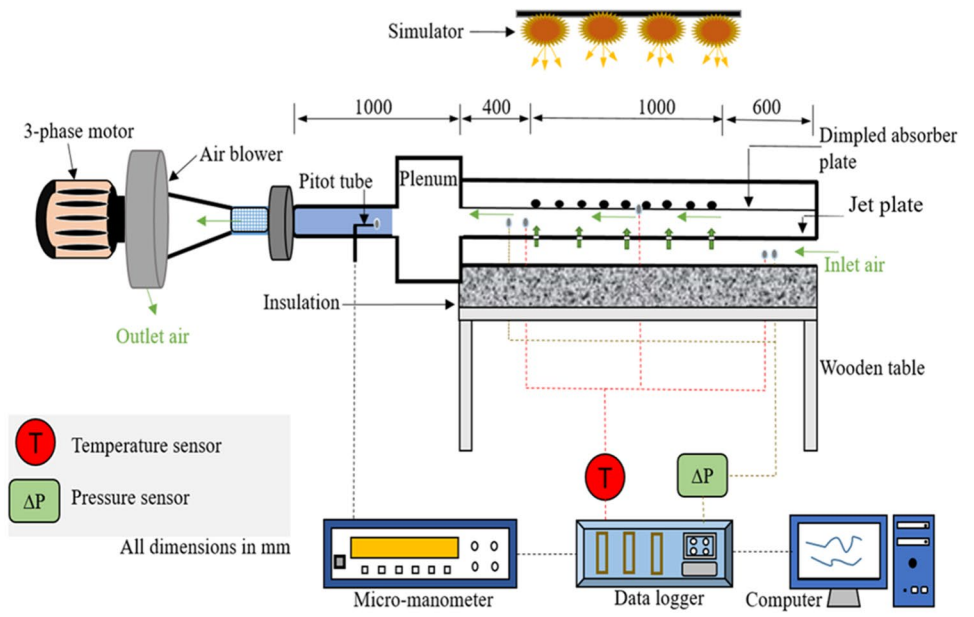
where A_{ab} is absorber plate surface area.

T_{abm} is bulk mean temperature of the absorber plate $T_{abm} = \frac{1}{15} \left(\sum_{i=1}^{15} T_{abmi} \right)$; T_{am} is mean temperature of the absorber plate $T_{am} = \frac{T_{ai} + T_{ao}}{2}$

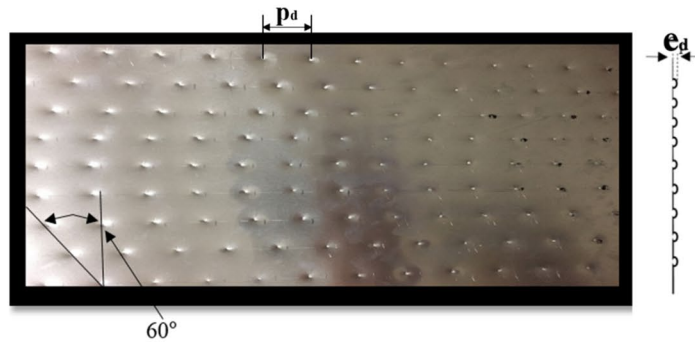
Fig. 1 **a** Pictographic view of the test facility, **b** graphical representation of test facility, **c** dimple-roughened absorber plate.



(a)



(b)



(c)

Table 1 Characteristics of apparatus used

| Component | Specification/Dimension |
|---------------------------|-----------------------------------|
| DAQ | 9–30/V @ 15/W, 10–90/% RH, 0.05/% |
| Pressure gauge | ± 0.13% (0–0.5 in. W.C.) |
| Air blower | 3400/rpm, 3 Φ 220/380/V |
| Pitot tube | Ø 3.2×150/mm |
| Solarimeter | 0–1/V output |
| Thermocouple (K-type) | ± 0.1%, – 60–1300 °C |
| Duct (mm) | 2000 (L)×252 (W)×25 (H) |
| Entry, exit sections (mm) | 600, 400 |
| Top cover (mm) | 2000 (L)×332 (W)×5 (T) |
| Impingement plate (mm) | 2000 (L)×290 (W)×5 (T) |
| Absorber plate (mm) | 2000 (L)×300 (W)×1 (T) |

The h_{ct} for the duct has been evaluated as

$$h_{ct} = \frac{Q_{uhg}}{A_{ab}(T_{abm} - T_{am})} \tag{5}$$

The Nusselt number, $Nu_{jd} = \frac{h_{ct}D_{hd}}{k_a}$ (6)

Where k_a is thermal conductivity of air.

The friction factor, $ff_{jd} = \frac{(\Delta P_d)}{2\rho_a L_t V_a^2}$ (7)

where ΔP_d is the differential pressure across the duct, and L_t is the length of the test section.

Fig. 2 a Position of thermocouples, b temperature variation of air inside the duct.

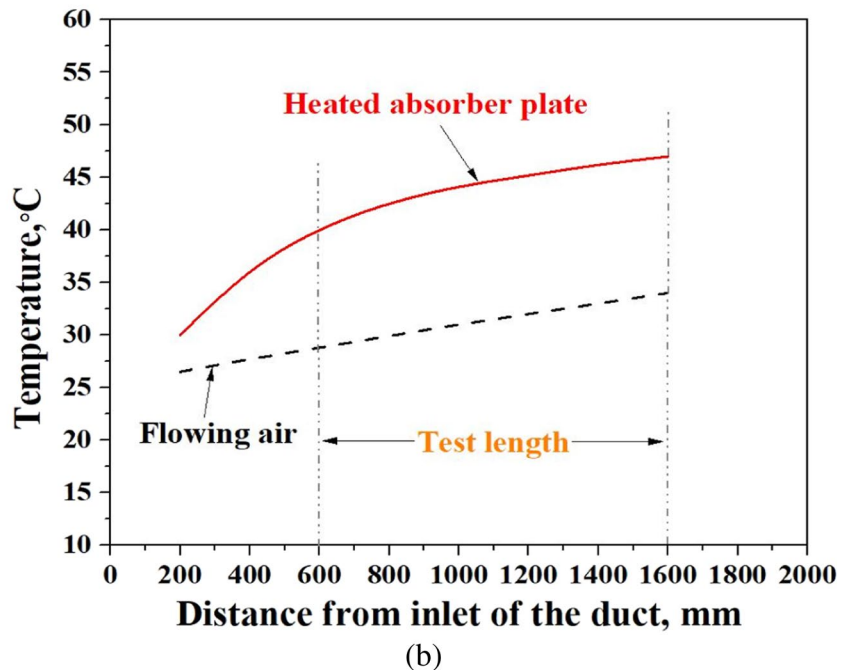
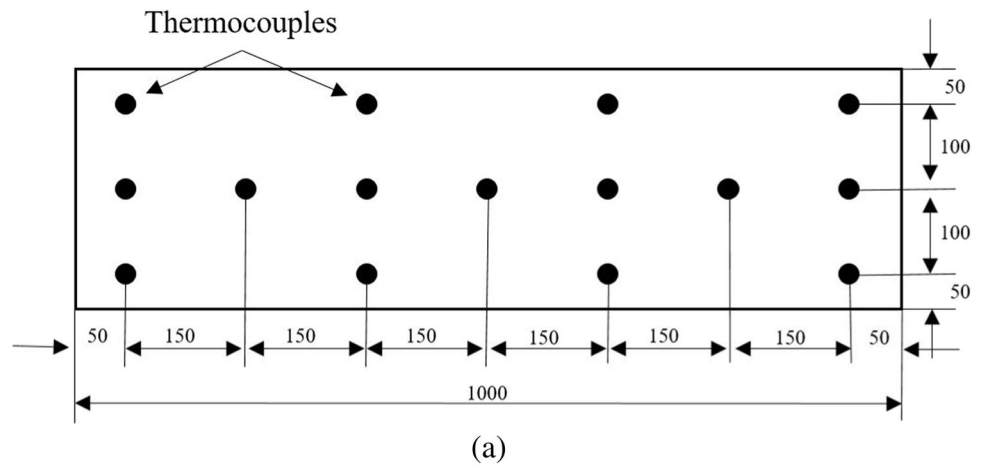


Table 2 Range of flow and geometric parameters

| Alternative | Re | α_{aa} | p_d/D_h | e_d/D_h | Alternative | Re | α_{aa} | p_d/D_h | e_d/D_h |
|-------------|--------|---------------|-----------|-----------|-------------|--------|---------------|-----------|-----------|
| A-1 | 15,000 | 30 | 0.27 | 0.016 | A-9 | 15,000 | 60 | 0.27 | 0.027 |
| A-2 | 15,000 | 30 | 0.54 | 0.021 | A-10 | 15,000 | 60 | 0.54 | 0.0324 |
| A-3 | 15,000 | 30 | 0.81 | 0.027 | A-11 | 15,000 | 60 | 0.81 | 0.016 |
| A-4 | 15,000 | 30 | 1.08 | 0.0324 | A-12 | 15,000 | 60 | 1.08 | 0.021 |
| A-5 | 15,000 | 45 | 0.27 | 0.021 | A-13 | 15,000 | 75 | 0.27 | 0.0324 |
| A-6 | 15,000 | 45 | 0.54 | 0.016 | A-14 | 15,000 | 75 | 0.54 | 0.027 |
| A-7 | 15,000 | 45 | 0.81 | 0.0324 | A-15 | 15,000 | 75 | 0.81 | 0.021 |
| A-8 | 15,000 | 45 | 1.08 | 0.027 | A-16 | 15,000 | 75 | 1.08 | 0.016 |

Experimental validation and uncertainty in measurement

Validation of SPSAC and jet impingement duct

To establish a comparative foundation with heat transfer and pressure losses concerning the Nusselt number and friction factor correlations stated in the literature, experimental tests proving the validity of the SPSAC test rig were performed. The obtained experimental results were compared with the respective correlation predictions. The Dittus–Boelter (Bhatti and Shah 1987) and the modified Blasius equation (Incropera et al. 2011), as presented in Eq. 8 and Eq. 9, were used to correlate the Nu_s and ff_s values determined in contradiction to the data obtained for the smooth absorber plate.

$$Nu_s = 0.023Re^{0.8}Pr^{-0.4} \tag{8}$$

$$ff_s = 0.085Re^{-0.25} \tag{9}$$

Figure 3 depicts an assessment of the experimental and expected values of Nu_s and ff_s as a function of Re. The attributes obtained for Nu_s and ff_s by execution testing on FPSAC and those achieved from the standard correlations are comparable, as shown in Fig. 3. The deviance of the experimental and correlation values of Nu_s and ff_s are within the ± 6 –10% range which validates the SPSAC experimental duct.

For the optimum parameters of the jet slot, the Nu_i and ff_i statistics for air impinged on a smooth absorber plate revealed through experimental research were compared with the values acquired from Chauhan and Thakur’s correlation (2013), as depicted in Eqs. 10 and 11.

$$Nu_i = 0.00166(Re)^{0.8512} \left(\frac{X_i}{D_{hd}}\right)^{0.1761} \left(\frac{Y_i}{D_{hd}}\right)^{0.141} \left(\frac{D_i}{D_{hd}}\right)^{-1.9854} \exp\left[-0.3498\left(\ln\left(\frac{D_i}{D_{hd}}\right)\right)^2\right] \tag{10}$$

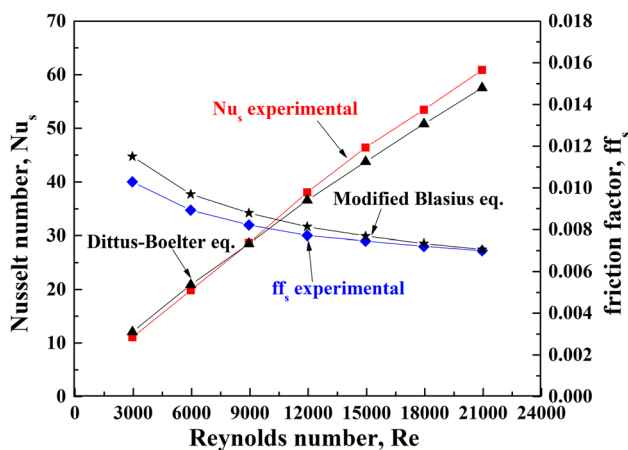


Fig. 3 Validation of FPSAC duct

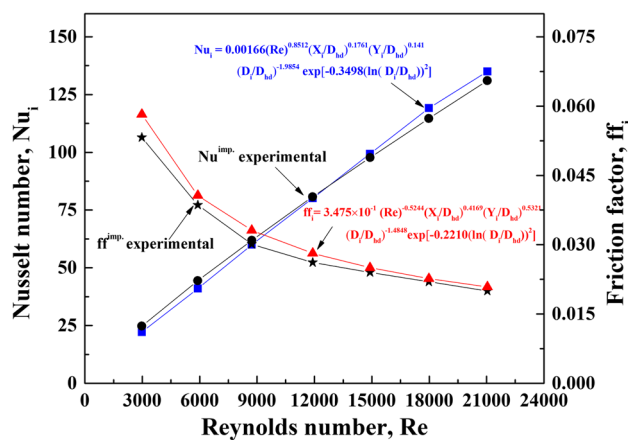


Fig. 4 Validation of jet impingement duct

$$ff_i = 3.475 \times 10^{-1} (\text{Re})^{-0.5244} \left(\frac{X_i}{D_{hd}}\right)^{0.4169} \left(\frac{Y_i}{D_{hd}}\right)^{0.5321} \left(\frac{D_i}{D_{hd}}\right)^{-1.4848} \exp \left[-0.2210 \left(\ln \left(\frac{D_i}{D_{hd}} \right) \right)^2 \right] \tag{11}$$

Figure 4 shows an evaluation of the experimental and correlated results of Nu_i and ff_i as a function of Re . The maximum deviation of the experimental values of Nu_i and ff_i values was within the range of ± 5 –9%. The good agreement shown by the experiment and the correlated values certifies that the accuracy of the data is hoarded with the aid of a test rig. The constant parameters of the jet slot considered are stream-wise pitch ratio (X_i/D_{hd}) = 1.079, span-wise pitch ratio (Y_i/D_{hd}) = 1.619, and jet diameter (D_i/D_{hd}) = 0.081.

Uncertainty in measurement

The values acquired through the examination may diverge from their real value since the existence of several factors that come into play during evaluation and recording. The uncertainty in the measurement is the alteration between the measured and real values. The uncertainties related to several instruments used in the data measurement are depicted in Table 3. Considering the errors in the measurements of the flow and geometric parameters, an uncertainty test was performed. The uncertainty was calculated in this investigation using the procedures described by Kline and McClintock (1953) and Moffat (1985). The following is a description of the technique for calculating uncertainty:

After the parameter is determined by employing thoroughly measured amounts, the uncertainty in the measurement of “y” is provided by

$$\frac{\delta y}{y} = \left[\left(\frac{\delta y}{\delta x_1} \delta x_1 \right)^2 + \left(\frac{\delta y}{\delta x_2} \delta x_2 \right)^2 + \left(\frac{\delta y}{\delta x_3} \delta x_3 \right)^2 + \dots + \left(\frac{\delta y}{\delta x_n} \delta x_n \right)^2 \right]^{1/2} \tag{12}$$

where $\delta x_1, \delta x_2, \delta x_3, \dots, \delta x_n$ are the possible errors in the measurement of $x_1, x_2, x_3, \dots, x_n$.

Table 3 Range of error of used instruments

| S.No | Instruments | Range | Least count | Accuracy |
|------|----------------------------------------|--------------|-------------|------------|
| 1 | Vernier caliper (mm) | 0–150 | 0.1 | ± 0.01 |
| 2 | Micro-manometer (Pa) | $\pm 5\ 000$ | 1 | ± 0.1 |
| 4 | K- thermocouple ($^{\circ}\text{C}$) | – 60– 1200 | – | ± 1.4 |
| 5 | Solarimeter (W/m^2) | 0–2000 | 5 | ± 0.01 |

δy is the total, and $\delta y/y$ is the comparative uncertainty. The uncertainty in the measurement of duct dimensions and process parameters are evaluated as.

A. Hydraulic diameter (D_{hd})

$$\frac{\delta D_{hd}}{D_{hd}} = \frac{4 \left[\left(\frac{\delta D_{hd}}{\delta H_d} \times \delta H_d \right)^2 + \left(\frac{\delta D_{hd}}{\delta W_d} \times \delta W_d \right)^2 \right]^{1/2}}{2 \times (W_d \times H_d) (W_d + H_d)^{-1}} \tag{13}$$

B. Area of the absorber plate (A_{ab})

$$\frac{\delta A_{ab}}{A_{ab}} = \left[\left(\frac{W_d \times \delta L_d}{W_d \times L_d} \right)^2 + \left(\frac{L_d \times \delta W_d}{W_d \times L_d} \right)^2 \right]^{1/2} \tag{14}$$

C. Reynolds number (Re)

$$\frac{\delta \text{Re}}{\text{Re}} = \left[\left(\frac{\delta V_a}{V_a} \right)^2 + \left(\frac{\delta \rho_a}{\rho_a} \right)^2 + \left(\frac{\delta D_{hd}}{D_{hd}} \right)^2 + \left(\frac{\delta \mu_a}{\mu_a} \right)^2 \right]^{1/2} \tag{15}$$

D. Useful heat gain (Q_{uhg})

$$\frac{\delta Q_{uhg}}{Q_{uhg}} = \left[\left(\frac{\delta m_a}{m_a} \right)^2 + \left(\frac{\delta C_p}{C_p} \right)^2 + \left(\frac{\delta T_{am}}{T_{am}} \right)^2 \right]^{1/2} \tag{16}$$

E. Heat transfer coefficient (h_{ct})

$$\frac{\delta h_{ct}}{h_{ct}} = \left[\left(\frac{\delta Q_{uhg}}{Q_{uhg}} \right)^2 + \left(\frac{\delta A_{ab}}{A_{ab}} \right)^2 + \left(\frac{\delta T_{am}}{T_{am}} \right)^2 \right]^{1/2} \tag{17}$$

F. Nusselt number (Nu_{jd})

$$\frac{\delta Nu_{jd}}{Nu_{jd}} = \left[\left(\frac{\delta h_{ct}}{h_{ct}} \right)^2 + \left(\frac{\delta D_{hd}}{D_{hd}} \right)^2 + \left(\frac{\delta k_a}{k_a} \right)^2 \right]^{1/2} \tag{18}$$

G. Friction factor (ff_{jd})

$$\frac{\delta ff_{jd}}{ff_{jd}} = \left[\left(\frac{\delta V_a}{V_a} \right)^2 + \left(\frac{\delta \rho_a}{\rho_a} \right)^2 + \left(\frac{\delta D_{hd}}{D_{hd}} \right)^2 + \left(\frac{\delta L_t}{L_t} \right)^2 + \left(\frac{\delta (\Delta P_d)}{\Delta P_d} \right)^2 \right]^{1/2} \tag{19}$$

Based on the precision of the equipment utilized and the data reduction procedure, the detailed uncertainties in the current examination for the firm and important properties are listed in Table 4.

Table 4 Range of uncertainty in the calculation of process parameters

| Parameter | Uncertainty |
|------------------------------------------------|-------------|
| Useful heat gain (Q_{uhg}) | ± 3.35 |
| Nusselt number (Nu_{jd}) | ± 4.57 |
| Reynolds number (Re) | ± 2.14 |
| Friction factor (f_{fd}) | ± 4.21 |
| Dimple heated plate temperature, T_{ab} (°C) | ± 2.5 |
| Velocity of air, V_a (m/s) | ± 0.92 |
| Differential pressure, ΔP_d (Pa) | ± 2.51 |
| Heat transfer coefficient (h_{ct}) | ± 3.58 |

Proposed methodology

The integrated AHP-MABAC technique is one of the finest design and optimization methods for evaluating control parameters individually to arrive at the best design values. It entails three main stages of the assessment process, as shown in Fig. 5.

Stage 1: determination of alternatives, criteria, and performance matrix

In the first stage, the alternatives and criteria for a given MCDM problem are specified. Thereafter, the specified alternatives and criteria are expressed in the form of a performance matrix. Generally, a performance matrix (U) for any MCDM problem with M alternatives ($A_i, i = 1, 2, \dots, M$) to be evaluated using N criteria ($C_j, j = 1, 2, \dots, N$) is constructed as

$$U = \begin{matrix} A_1 \\ A_2 \\ \vdots \\ A_M \end{matrix} \begin{bmatrix} C_1 & C_2 & C_3 & \dots & C_N \\ u_{11} & u_{12} & u_{13} & \dots & u_{1N} \\ u_{21} & u_{22} & u_{23} & \dots & u_{2N} \\ \vdots & \vdots & \vdots & \ddots & \vdots \\ u_{M1} & u_{M2} & u_{M3} & \dots & u_{MN} \end{bmatrix} \quad (20)$$

An element u_{ij} of the performance matrix signifies the performance score of the i^{th} alternative A_i , concerning the j^{th} criterion C_j .

Stage 2: AHP method for weight calculation

AHP is widely used to address the relative importance of activities in an MCDM problem. For this, a pairwise comparison matrix was constructed using a standardized comparison scale of 9 points. For N criteria, $C_j, j = 1, 2, \dots, N$, the pairwise comparison matrix (P_{NN}) is constructed as

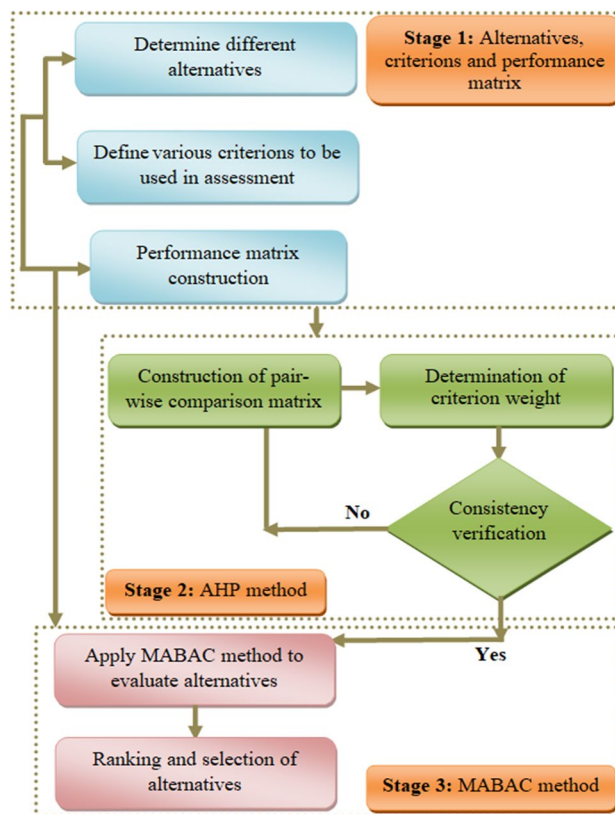


Fig. 5 Architecture of the proposed AHP-MABAC methodology

$$P_{NN} = \begin{matrix} C_1 \\ C_2 \\ \vdots \\ C_N \end{matrix} \begin{bmatrix} C_1 & C_2 & C_3 & \dots & C_N \\ p_{11} & p_{12} & p_{13} & \dots & p_{1N} \\ p_{21} & p_{22} & p_{23} & \dots & p_{2N} \\ \vdots & \vdots & \vdots & \ddots & \vdots \\ p_{N1} & p_{N2} & p_{N3} & \dots & p_{NN} \end{bmatrix} \quad p_{ij} = 1 \text{ if } i = j, p_{ji} = \frac{1}{p_{ij}}, p_{ij} \neq 0 \quad (21)$$

Every element of the constructed comparison matrix $p_{ij}(i, j = 1, 2, \dots, N)$ is a measure of the criterion weight. As a result, the criterion weights are determined by the right eigenvector (w), which corresponds to the leading eigenvalue.

$$(P_{NN})_w = \lambda_{\max} w \quad (22)$$

It has been reported in the literature that AHP superiority is firmly associated with the reliability of pairwise comparison outcomes. For a completely consistent pairwise comparison matrix, the matrix should have $\lambda_{\max} = N$ and a rank of 1. By stabilizing any of the rows or columns in the table, the weights can be found for the constructed pairwise comparison matrix. Finally, consistency confirmation was

performed to ensure that the assessments were adequately reliable. The consistency ratio (CR) is considered as

$$\text{Consistency Ratio (CR)} = \frac{\lambda_{\max} - N}{N - 1} \times \frac{1}{RI} \quad (23)$$

where RI is the random index of the matrix, and its value is decided according to the order of the constructed pairwise comparison matrix. The results of the AHP are regarded as reasonable if the assessment of CR is less than the approved maximum limit of 0.1. The pairwise comparison matrix is re-created to increase consistency if the CR value exceeded 0.1.

Stage 3: MABAC approach for final ranking

In the MABAC method, first, the constructed performance matrix is normalized to make different entities comparable using the following equations:

$$U_{ij}^* = \frac{u_{ij}}{u_i^+ - u_i^-}, \text{ the higher the value of } j, \text{ the better, and} \quad (24)$$

$$U_{ij}^* = \frac{u_{ij} - u_i^+}{u_i^- - u_i^+}, \text{ the lower the value of } j, \text{ the better.}$$

where U_{ij}^* denotes the normalized value of the i th alternative and j th criterion of the performance matrix. Further, $u_i^+ = \max(u_1, u_2, u_3, \dots, u_M)$, and $u_i^- = \min(u_1, u_2, u_3, \dots, u_M)$.

Thereafter, weighted normalized performance matrix is structured as

$$\varpi_{ij} = w_j + (U_{ij}^* \times w_j); i = (1, 2 \dots M), j = (1, 2 \dots N) \quad (25)$$

The border approximation area matrix is structured by employing the following equation:

$$\mathfrak{R}_j = \left(\prod_{i=1}^M \varpi_{ij} \right)^{1/M} \quad ; j = (1, 2 \dots N) \quad (26)$$

The distance amid the weighted normalized performance matrix and border approximation area matrix is calculated as

$$d_{ij} = \varpi_{ij} - \mathfrak{R}_j; i = (1, 2 \dots M), j = (1, 2 \dots N) \quad (27)$$

Finally, the total distance of the individual alternative from the approximate border area is calculated using the following equation:

$$\Psi_i = \sum_{j=1}^N d_{ij}; i = (1, 2 \dots M) \quad (28)$$

The ranking of alternatives is accomplished on the computed value of Ψ_i , and the alternative with the maximum Ψ_i value is ranked 1st, while the alternative with the lowest Ψ_i value is ranked last.

Results and discussion

Experiment results

This investigation aimed to determine the heat transfer characteristics of JIDRSAC. However, dimple-roughened surfaces are more noticeable for enhancing convective heat transfer and keeping friction losses low as compared with conventional SAC; they were therefore selected for investigation. The levels of the selected control factors (CF) used in the experiment are listed in Table 5. These levels are methodically selected from a rational set of CFs that can impact the thermal and hydraulic performance of the JIDRSAC. The results indicate that the dimple roughness arranged in an arc-shaped manner has a robust inclination to release heat away from the roughened absorber plate, yet friction losses occur because of the formation of turbulence inside the duct. Therefore, it is essential to examine both Nu_{jd} and ff_{jd} in order to simultaneously take the JIDRSAC performance evaluation into account. When assessing the energy quality associated with a JIDRSAC, it is possible to account for the value of usable energy output, friction losses, and other losses that occur within a JIDRSAC. Altfield et al. (1988) proposed a method for establishing a link between the usable energy output and pressure losses in a JIDRSAC based on the second law of thermodynamics. The exergetic efficiency (η_{ex}) measures how much work a system can complete with the least amount of energy input, making it important for analyzing a JIDRSAC's performance.

$$\eta_{ex} = \frac{\eta_{th} \eta_c - P_m (1 - \eta_c)}{(1 - T_a / T_{sun})} \quad (29)$$

where P_m is the power spent to sustain airflow in the duct and is expressed as

$$P_m = \frac{m_a \times \Delta P_d}{\rho_a}$$

The Nu_{jd} , ff_{jd} , and η_{ex} PDCs have been used, and they were all measured and weighed. The combined AHP-MABAC methodology is used to optimize the dimple roughness and flow parameters in a JIDRSAC, where Nu_{jd} and ff_{jd} reflect the thermal and hydraulic behavior of the JIDRSAC and η_{ex} provides information on the JIDRSAC's overall performance. The values of Nu_{jd} , ff_{jd} , and η_{ex} for sixteen alternatives—parametric sets of dimple-roughened absorber plate taken into consideration for the JIDRSAC at $Re = 15,000$ are shown in Table 6. Figure 6a and b depicts the selected PDC values for the designated alternatives. The PDCs of the analyzed system is dependent on the CF and flow characteristics, as the alternatives considered are operational deviations of these parameters. The relay behavior of selected PDCs indicates

Table 5 Details of system control factors

| Control Factor (CF) | Level | | | |
|------------------------|-------|-------|-------|--------|
| | I | II | III | IV |
| CF-1 (α_{aa}) | 30 | 45 | 60 | 75 |
| CF-2 (p_d/D_h) | 0.27 | 0.54 | 0.81 | 1.08 |
| CF-3 (e_d/D_h) | 0.016 | 0.021 | 0.027 | 0.0324 |

that the modification in the absorber plate configuration has produced a significant change concerning their results.

As a result, it is essential to examine both Nu_{jd} and ff_{jd} to take into consideration the simultaneous concern in performance evaluation. As can be seen from the results presented in Table 5, alternative A-9 has the uppermost value of PDC-1, while the lowest is for A-16. In addition, for PDC-2, the highest value was at A-10 and the lowest at A-16. Therefore, it is impossible to provide an alternative for any absorber in which PDC-1 is the greatest and PDC-2 is the lowest at the same time. Therefore, PDC-3 (η_{ex}) plays a vital role in considering the best alternative for the current study. The analytical results in the form of PDCs show that the dimple roughness parameters p_d , α_{aa} , and e_d all have a substantial impact on the thermal and hydraulic characteristics of a JIDRSAC. Whereas PDC-1 increases as the value of CF-1 increases from 30° to 60°, it starts to decline and beyond 60°, as observed in the case of the set of alternatives A-1, A-5, A-9, and A-13. This is because of the presence of dimple roughness at the air stream’s departure inside the duct, and the expansion of the secondary vortices mixed uniformly to produce the maximum value of α_{aa} . In addition, the variation in CF-3 shows an enhancement in PDC-1 with an increase in flow rate. This is because the convective heat transfer coefficient is truncated at the fundamental edge of the dimple roughness but high at the succeeding edge. For the set of alternatives A-9, A-10, A-11, and A-12, as the value of CF-2 surges, the value of PDC-3 declines. This is because the number of vortex generations may decline when the value of p/D_{hd} increases owing to a decrease in heat transfer. The absorber surface inside the stagnation zone affects the flow,

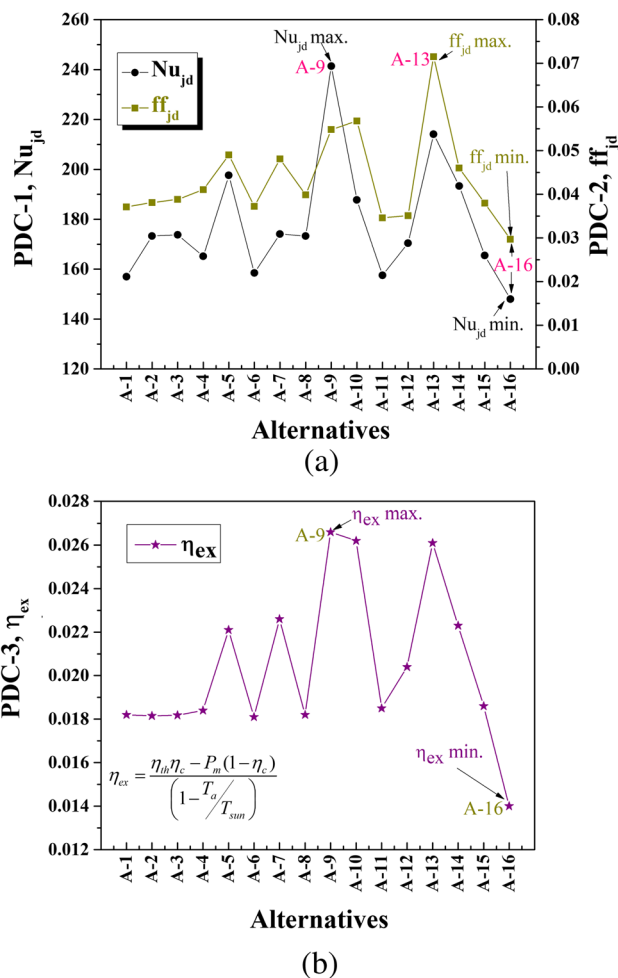


Fig. 6 Variation of **a** PDC-1 & PDC-2, and **b** PDC-3 with alternatives

and the axial velocity of the jet decelerates and bounces along the radial path. The flow separation zone behaves as a free shear layer, which is very unstable, and the dimples on the absorber plate create a flow detachment zone, which becomes unstable by creating vortices. The vortices will not only support the entrainment of fast mainstream flow from

Table 6 Experimental data of the selected PDCs

| Alternative | PDC-1 | PDC-2 | PDC-3 | Alternative | PDC-1 | PDC-2 | PDC-3 |
|-------------|---------|----------|---------|-------------|---------|----------|--------|
| A-1 | 157.006 | 0.037124 | 0.0182 | A-9 | 241.370 | 0.054824 | 0.0266 |
| A-2 | 173.236 | 0.038124 | 0.01815 | A-10 | 187.788 | 0.056791 | 0.0262 |
| A-3 | 173.736 | 0.038824 | 0.01818 | A-11 | 157.541 | 0.034625 | 0.0185 |
| A-4 | 165.142 | 0.041067 | 0.0184 | A-12 | 170.448 | 0.035114 | 0.0204 |
| A-5 | 197.614 | 0.04902 | 0.0221 | A-13 | 214.102 | 0.071532 | 0.0261 |
| A-6 | 158.443 | 0.03725 | 0.0181 | A-14 | 193.326 | 0.045992 | 0.0223 |
| A-7 | 174.074 | 0.048098 | 0.0226 | A-15 | 165.452 | 0.037971 | 0.0186 |
| A-8 | 173.236 | 0.039874 | 0.0182 | A-16 | 147.965 | 0.029684 | 0.0140 |

the exterior but also assist in the acquittal of the low heat transfer zone. Owing to the presence of a low-pressure zone at the start of the dimple, the hasty mainstream flow travels downward. After a jet airflow impacts the dimple, the flow splits into two, with one flow salvaging inside the dimple and the former moving out of the dimple. However, as the air-flow rate increases, the increase in heat transmission is conveyed by a surge in the friction factor, which has an adverse effect on the performance of the JIDRSAC. The results also showed that with an increase in CF-1, PDC-1 increases, and PDC-2 increases first up to level-3 followed by a decline at the next level. However, PDC-2 increased up to its maximum value with an increase in CF-1. For reasonably good performance of the JIDRSAC system, PDC-1 and PDC-3 must be as high as feasible, while PDC-2 must be as low as possible. Amid the experimented dimple-roughened absorber plate arrangements for $Re = 15,000$, alternative A-9 consists of a parametric set of $p_d/D_h = 0.27$, $\alpha_{aa} = 60^\circ$, and $e_d/D_h = 0.027$ holds the optimal value of PDC-3. Although the alternative A-13 holds the maximum value of PDC-2 with a set of parameters $p_d/D_h = 0.27$, $\alpha_{aa} = 75^\circ$, and $e_d/D_h = 0.0324$, while the lowest PDC-2 is for A-16.

Purpose of PDC weights

In an MCDM problem, the AHP is most commonly utilized to address the relative importance of activities. It provides the decision to be organized hierarchically to reduce complexity and show relationships between different factors. This can also combine qualitative and quantitative aspects in a single-decision framework. As shown in Eqs. 21 and 22, a pairwise comparison matrix is created, and every element of the matrix p_{ij} is the measure of standard weight. The PDCs were associated pairwise to assess the intensity of significance for individual PDC using a 9-point scale after establishing the decision hierarchy for the subject, with 1 being correspondingly significant and 9 with the further being particularly more significant. The responses were logged on a comparison matrix, and the priority vectors were calculated using basic matrix algebra procedures (Saaty 2008; Ishizaka and Labib 2011). The pairwise comparison matrix presented in Table 7 is accomplished by allocating each component of the matrix by the sum of its columns. The weight of PDC-1 (0.540) was found to be maximally trailed by the weight of PDC-3 (0.297) and PDC-2 (0.163). To obtain λ_{\max} , the average of these values is computed by dividing the respective elements of the weighted sum matrix by their significance vector element. To define the consistency of the matrix, some significant consistency parameters were considered, that is, $\lambda_{\max} = 3.009$, consistency ratio (CR) = 0.0079, and random consistency index (RI) = 0.58. At the point where the CR appears to be less than 0.1, the matrix judgment becomes significant. As a result, the pairwise comparison

Table 7 Pairwise comparison matrix and results of AHP

| | Pairwise comparison matrix | | | Results of AHP | |
|-------|----------------------------|-------|-------|--------------------------|--------|
| | PDC-1 | PDC-2 | PDC-3 | Consistency parameters | Weight |
| PDC-1 | 1 | 3 | 2 | $\lambda_{\max} = 3.009$ | 0.540 |
| PDC-2 | 1/3 | 1 | 1/2 | RI = 0.58 | 0.163 |
| PDC-3 | 1/2 | 2 | 1 | CR = 0.0079 | 0.297 |

matrix was deemed steady; therefore, the weights were incorporated in the MABAC method.

Classification of the final rank

The PDC weights were obtained using the AHP approach, and the remaining steps of the AHP-MABAC process were utilized to rank the created alternatives according to their overall performance. In compliance with the MABAC procedure outlined in stage-3 of “[Experimental validation and uncertainty in measurement](#)” section, the individual unit of the decision matrix is standardized in the assortment of 0–1 by Eq. 24. After calculating the normalized matrix, a weighted normalized matrix is created for each criterion by multiplying each column of the normalized decision matrix U_{ij}^* with the weighted association criterion ϖ_{ij} equivalent to that column using Eq. 25. The resulting normalized matrix and weighted normalized matrix for the MABAC approach are listed in Table 8.

The border approximation area matrix is presented in Table 9 and is planned in accordance with the steps followed for the MABAC approach given in Eq. 26. The table specifies that the value of the border approximation area for PDC-1 is the highest (0.7033), and the lowest is 0.2688 for PDC-3. Consequently, the distance between the weighted normalized matrix and the border approximation area matrix of each alternative is evaluated, as shown in Eq. 27. Finally, using Eq. 28, the total distance (Ψ_i) of each alternative from the approximate border area was determined and is presented in Table 10. Based on the Ψ_i values against the alternatives, the concluding ranking of the alternatives concerning their overall performance is obtained and shown in Table 10. The best alternative among the 16 alternatives is A-9, with a rank of 1, as shown in Fig. 7. For alternative A-9, the values of the selected PDCs are PDC-1 = 0.3767, PDC-2 = -0.0407, PDC-3 = 0.1478, and Ψ_i is maximum (0.4838). The alternatives can be organized in ascending order as A-9 < A-13 < A-10 < A-5 < A-7 < A-12 < A-3 < A-2 < A-8 < A-15 < A-4 < A-11 < A-6 < A-1 < A-16. Alternative A-16 has the lowest rank among all, with a Ψ_i value of -0.2484. From this optimization of JIDRSAC by utilizing the AHP-MABAC technique, it is clear that the dimple roughness parameter, that is, $p_d/$

Table 8 Normalized and weighted normalized matrix

| Alternatives | Normalized matrix | | | Weighted normalized matrix | | |
|--------------|-------------------|--------|--------|----------------------------|--------|--------|
| | PDC-1 | PDC-2 | PDC-3 | PDC-1 | PDC-2 | PDC-3 |
| A-1 | 0.0968 | 0.8230 | 0.3256 | 0.5923 | 0.2971 | 0.3937 |
| A-2 | 0.2706 | 0.7990 | 0.3256 | 0.6861 | 0.2932 | 0.3937 |
| A-3 | 0.2759 | 0.7823 | 0.3256 | 0.6890 | 0.2905 | 0.3937 |
| A-4 | 0.1838 | 0.7273 | 0.3411 | 0.6393 | 0.2815 | 0.3983 |
| A-5 | 0.5315 | 0.5383 | 0.6279 | 0.8270 | 0.2507 | 0.4835 |
| A-6 | 0.1121 | 0.8182 | 0.3178 | 0.6005 | 0.2964 | 0.3914 |
| A-7 | 0.2794 | 0.5598 | 0.6667 | 0.6909 | 0.2542 | 0.4950 |
| A-8 | 0.2706 | 0.7560 | 0.3256 | 0.6861 | 0.2862 | 0.3937 |
| A-9 | 1.0000 | 0.3995 | 0.9767 | 1.0800 | 0.2281 | 0.5871 |
| A-10 | 0.4263 | 0.3517 | 0.9922 | 0.7702 | 0.2203 | 0.5917 |
| A-11 | 0.1025 | 0.8828 | 0.3488 | 0.5953 | 0.3069 | 0.4006 |
| A-12 | 0.2407 | 0.8708 | 0.4961 | 0.6700 | 0.3049 | 0.4443 |
| A-13 | 0.7080 | 0.0000 | 1.0000 | 0.9223 | 0.1630 | 0.5940 |
| A-14 | 0.4857 | 0.6100 | 0.6434 | 0.8023 | 0.2624 | 0.4881 |
| A-15 | 0.1872 | 0.8014 | 0.3566 | 0.6411 | 0.2936 | 0.4029 |
| A-16 | 0.0000 | 1.0000 | 0.0000 | 0.5400 | 0.3260 | 0.2970 |

$D_h = 0.27$, $\alpha_{aa} = 60^\circ$, and $e_d/D_h = 0.027$ is the best selection under these circumstances, taking into account three PDCs at the same time.

Sensitivity analysis

The weight of the PDCs used in decision-making has a significant impact on the ranking outcomes. The weighting results of the AHP approach may be subject to change under various conditions, for example, internal changes in the pairwise comparison matrix. As a result, sensitivity analysis should be considered while evaluating the robustness of the presented MCDM results. The sensitivity analysis of the proposed AHP-MABAC approach was performed by generating new weights of the selected three PDCs (Nu_{jd} , ff_{jd} , and η_{ex}) in steps and analyzing their impact on the rankings results. The new weights were determined by adjusting the weight of a PDC in four steps ($\pm 10\%$, $\pm 20\%$, $\pm 30\%$, and $\pm 50\%$). The weights of the remaining two PDCs were correspondingly changed so that the total weight of all PDCs remained 1. In total, 24 situations were generated, with the relevant ranking results shown in Fig. 8.

Analyzing Fig. 8, it can be concluded that changing the weight of the selected PDCs (Nu_{jd} , ff_{jd} , and η_{ex}) in four steps will not produce any significant changes in the rankings of the

alternatives. In all 24 scenarios, the A-9 remains the first-ranked alternative, whereas the A-16 remains the last-ranked alternative. The alternative A-13 remains the second-ranked except when the weight of Nu_{jd} (PDC-1) is reduced by 50%, where second-ranked and the third-ranked alternatives swap places. The ranking results found most sensitive when the Nu_{jd} (PDC-1) weight is reduced by 50%, the ranking of the alternative A-8 goes down by two places, while the ranking of alternative A-11 improved by two places. Similarly, alternative A-8 loses its ranking by two places when the weight of ff_{jd} (PDC-2) is

Table 10 Distance from border approximate area and ranking of alternatives

| Alternatives | PDC-1 | PDC-2 | PDC-3 | Ψ_i | Ranking |
|--------------|---------------|----------------|---------------|---------------|----------|
| A-1 | -0.1110 | 0.0283 | -0.0456 | -0.1283 | 15 |
| A-2 | -0.0172 | 0.0244 | -0.0456 | -0.0384 | 9 |
| A-3 | -0.0143 | 0.0217 | -0.0456 | -0.0382 | 8 |
| A-4 | -0.0640 | 0.0127 | -0.0410 | -0.0923 | 12 |
| A-5 | 0.1237 | -0.0181 | 0.0442 | 0.1498 | 4 |
| A-6 | -0.1028 | 0.0276 | -0.0479 | -0.1231 | 14 |
| A-7 | -0.0124 | -0.0146 | 0.0557 | 0.0287 | 6 |
| A-8 | -0.0172 | 0.0174 | -0.0456 | -0.0454 | 10 |
| A-9 | 0.3767 | -0.0407 | 0.1478 | 0.4838 | 1 |
| A-10 | 0.0669 | -0.0485 | 0.1524 | 0.1708 | 3 |
| A-11 | -0.1080 | 0.0381 | -0.0387 | -0.1086 | 13 |
| A-12 | -0.0333 | 0.0361 | 0.0050 | 0.0078 | 7 |
| A-13 | 0.2190 | -0.1058 | 0.1547 | 0.2679 | 2 |
| A-14 | 0.0990 | -0.0064 | 0.0488 | 0.1414 | 5 |
| A-15 | -0.0622 | 0.0248 | -0.0364 | -0.0738 | 11 |
| A-16 | -0.1633 | 0.0572 | -0.1423 | -0.2484 | 16 |

Table 9 The border approximate area matrix

| Border approximate area matrix | | |
|--------------------------------|--------|--------|
| C-1 | C-2 | C-3 |
| 0.7033 | 0.2688 | 0.4393 |

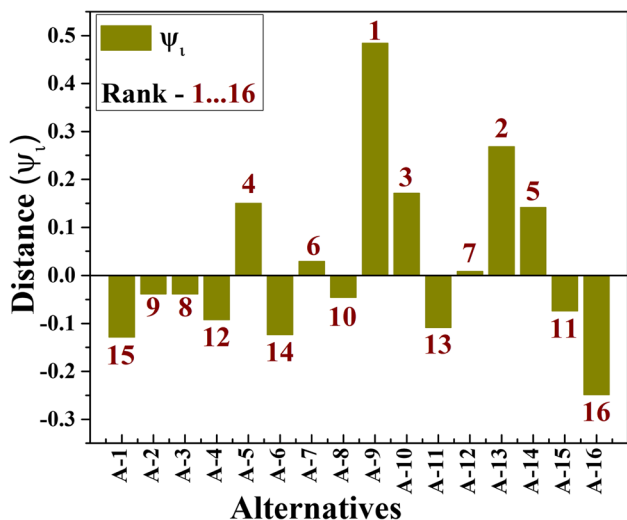
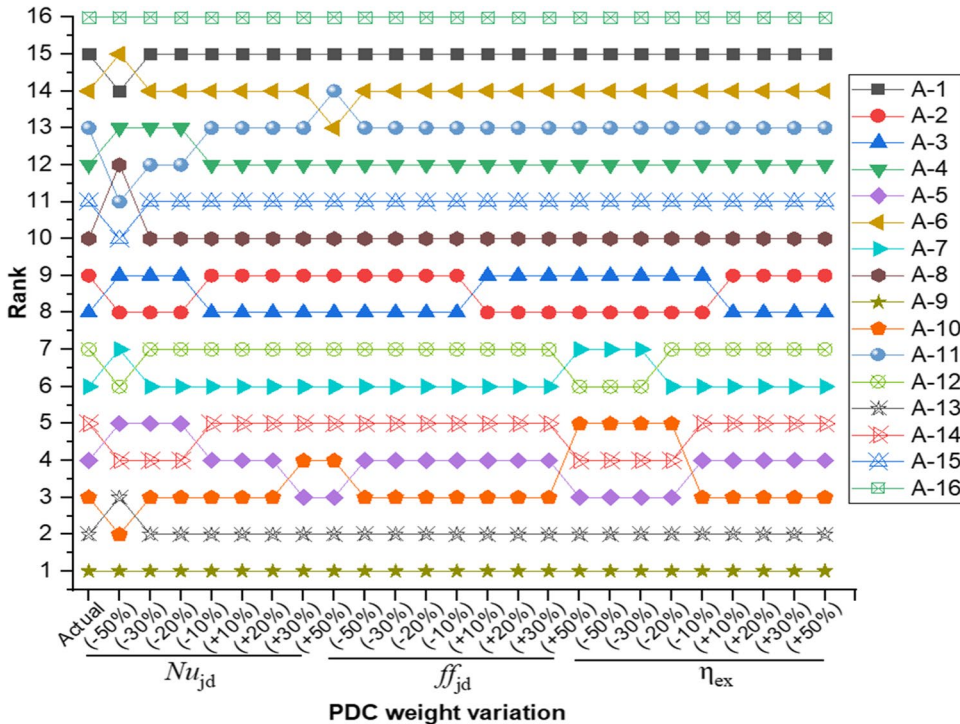


Fig. 7 Ranking of selected alternatives

increased by 50%, and PDC-3 (η_{ex}) is reduced by 20 to 50%. Apart from these significant changes, it is possible to see that the alternative go up or down by one place. However, these changes do not significantly affect the final results of the model, which is also confirmed by determining the Spearman correlation coefficient value using the following formula,

$$\text{Spearman correlation coefficient} = 1 - \frac{6 \sum_{i=1}^M \nabla_i^2}{M(M^2 - 1)} \quad (30)$$

Fig. 8 Sensitivity analysis



Here, ∇_i = Difference of actual rank and rank achieved with PDC weight variation; M = Alternatives.

The Spearman correlation coefficient remained more than 0.97 for all cases, signifying a strong correlation. It can be concluded from the sensitivity results that the acquired ranking is valid and reliable.

Furthermore, Fig. 9 shows the enhancement in Nu_{jd} and ff_{jd} compared with the SPSAC and jet impingement duct. When the jet impingement SAC is compared to a SPSAC, the Nu_i is enhanced by 2.16–2.81, and the ff_i is enhanced by 3.35–5.95. In addition, the present model, that is, JIDRSAC, is compared with the jet impingement SAC, which shows the augmentation in the Nu_{jd} and the ff_{jd} in the range of 0.55–0.80 and 0.05–0.15, respectively. Thus, it can be stated that the combined technique of air impinging vertically on the dimple-roughened absorber surface can transmit a greater value of thermal energy from the absorber surface compared to the SPSAC and jet impingement SAC. However, it also leads to a rise in pressure losses, which is anticipated to rise the friction factor.

Conclusions

This study examined the use of AHP-MABAC, an MCDM optimization technique, to determine the best dimple-roughened plate parameter arrangement in a JIDRSAC. The performance of JIDRSAC was investigated with

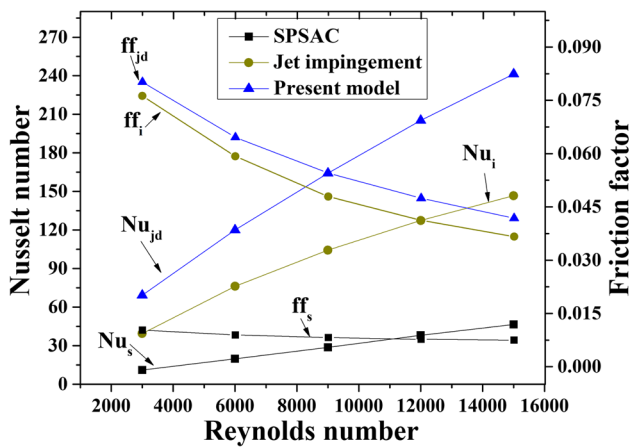


Fig. 9 Augmentation in Nu_{jd} and ff_{jd} at optimal CF arrangement

respect to convective heat transfer and friction loss features, and the performance criteria were assessed, revealing a distinct inclination for each of the 16 alternatives considered. The responses were classified into three categories: PDC-1, PDC-2, and PDC-3. The AHP-MABAC model was used to evaluate the best set of CFs to minimize friction losses and increase the convection heat transfer rate from the absorber plate to the flowing air. The CFs, which are the geometric parameters of the dimple roughness, have been characterized as p_d/D_h , α_{aa} , and e_d/D_h . The outcomes of this study can be useful in a variety of disciplines, including solar-based studies and thermal schemes, for the evaluation and optimization of the combined technique among desirable parameters for maximum performance. Based on the outcomes of the investigation, the following conclusions were drawn:

1. The maximum value of the total distance (Ψ_i) of individually alternatives from the approximate border area defines the rank of the alternatives. A-9, with the highest value of $\Psi_i = +0.4838$, has a rank of 1, while A-16 ranked last with the lowest value of $\Psi_i = -0.2484$.
2. Alternative holds the maximum value of Nu_{jd} and η_{ex} with a set of parameters $p_d/D_h = 0.27$, $\alpha_{aa} = 60^\circ$, and $e_d/D_h = 0.027$.
3. The parameter α_{aa} dominates in predicting the maximum value of the PDCs. The value of Nu_{jd} increases as the value of α_{aa} increases from 30° to 60° , and it starts to decline beyond 60° , as observed in the case of the set of alternatives A-1, A-5, A-9, and A-13.
4. Alternatives A-1, A-2, A-3, and A-4 indicate that ff_{jd} increases as the value of parameter e_p/D_h increases. This is because a secondary flow was produced along with the appearance of dimples as the value of e_p/D_h increased, and the power requisite to pump air through the JIDRSAC increased.

5. JIDRSAC compared to the jet impingement SAC, exhibits an increase in Nu_{jd} and ff_{jd} in the range of 0.55–0.80 and 0.05–0.15, respectively.
6. The validation of ranks generated via AHP-MABAC through sensitivity analysis of the PDCs are impermeable by the alteration in criteria weight.

Author contribution M.S, R.C, and S.C.K are contributed equally to the groundwork, idea, methodology, properties, formal investigation, writing—original draft preparation, review, and editing, and investigation; T.S, R.P, and S.C.K are contributed in scrutiny, review, and editing of the manuscript; S.C.K—supervision.

Funding This work was supported by the 2022 Yeungnam University Research Grant.

Data availability The datasets used and analysed during the current study are available from the corresponding author on reasonable request.

Declarations

Ethics approval Authors are attested that this paper has not been published elsewhere, the work has not been submitted simultaneously for publication elsewhere, and the results presented in this work are true and not manipulated.

Consent to participate All the individual participants involved in the study have received informed consent.

Consent for publication The participant has consented to the submission of the study to the journal.

Competing interest The authors declare no competing interests.

References

Abdollahpour A, Ghasempour R, Kasaeian A, Ahmadi MH (2020) Exergoeconomic analysis and optimization of a transcritical Co2 power cycle driven by solar energy based on nanofluids with liquified natural gas as its heat sink. *J Therm Anal Calorim* 139:451–473. <https://doi.org/10.1007/s10973-019-08375-6>

Abdul D, Wenqi J, Tanveer A (2022) Prioritization of renewable energy source for electricity generation through AHP-VIKOR integrated methodology. *Renewable Energy* 184:1018–1032. <https://doi.org/10.1016/j.renene.2021.10.082>

Altfeld K, Leiner W, Febig M (1988) Second law optimization of flat-plate solar air heaters Part I: the concept of net exergy flow and the modeling of solar air heaters. *Sol Energy* 41:127–132

Arafa S (2017) Community-based renewable energy education and training for sustainable development, 12th International symposium on renewable energy education proceedings, Sweden

ASHRAE Standard 93 (2003) Method of testing to determine the thermal performance of solar collectors. Atlanta, GA: American Society of Heating, Refrigeration, and Air Conditioning Engineers

Azari P, Lavasani AM, Rahbar N, Yazdi ME (2021) Performance enhancement of a solar still using a V-groove solar air collector-experimental study with energy, exergy, enviroeconomic, and

- exergoeconomic analysis. *Environ Sci Pollut Res* 28:65525–65548. <https://doi.org/10.1007/s11356-021-15290-7>
- Bhatti MS, Shah RK (1987) Turbulent and transition flow convective heat transfer. *Handbook of single-phase convective heat transfer*. John Wiley and Sons, New York
- Bertolini M, Braglia M, Carmignani G (2006) Application of the AHP methodology in making a proposal for a public work contract. *Int J of Project Mang* 5:422–430
- Biswas TK, Saha P (2019) Selection of commercially available scooters by new MCDM method. *Intl J Data Netw Sci* 3(2):137–144
- Bojanic D, Kovac M, Bojanic M, Ristic V (2018) Multi-criteria decision-making in a defensive operation of the guided anti-tank missile battery: an example of the hybrid model fuzzy ahp – mabac. *Decision Making: Appl Manag Eng* 1(1):51–66
- Bhushan B, Singh R (2011) Nusselt number and friction factor correlations for solar air heater duct having artificially roughened absorber plate. *Sol Energy* 85:1109–1118
- Chauhan R, Kim SC (2019a) Thermo-hydraulic characterization and design optimization of dimpled/ protruded absorbers in solar heat collectors. *Appl Therm Eng* 154:217–227
- Chauhan R, Kim SC (2019b) Effective efficiency distribution characteristics in protruded/dimpled arc plate solar thermal collector. *Renewable Energy* 138:955–963
- Chauhan R, Singh T, Thakur NS, Patnaik A (2016) Optimization of parameters in solar thermal collector provided with impinging air jets based upon preference selection index method. *Renewable Energy* 99:118–126
- Chauhan R, Singh T, Kumar N, Patnaik A, Thakur NS (2017a) Experimental investigation and optimization of impingement jet solar thermal collector by Taguchi method. *Appl Therm Eng* 116:100–109
- Chauhan R, Singh T, Tiwari A, Patnaik A, Thakur NS (2017b) Hybrid Entropy-TOPSIS approach for energy performance prioritization in a rectangular channel employing impinging air jets. *Energy* 134:360–368
- Chauhan R, Thakur NS (2014) Investigation of the thermohydraulic performance of impinging jet solar air heater. *Energy* 68:255–261
- Chauhan R, Thakur NS (2013) Heat transfer and friction factor correlations for impinging jet solar air heater. *Exp Therm Fluid Sci* 44:760–767
- Duffie JA, Beckman WA (2013) *Solar engineering of thermal processes*, 4th edn. Wiley, New York
- Gielen D, Boshell F, Saygin D, Bazilian MD, Wagner N (2019) The role of renewable energy in the global energy transformation. *Energy Strat Rev* 24:38–50
- Goel AK, Singh SN, Prasad BN (2021) Performance investigation and parametric optimization of an eco-friendly sustainable design solar air heater. *IET Renew Power Gener* 15:2645–2656
- Goel AK, Singh SN (2020a) Influence of fin density on the performance of an impinging jet with fins type solar air heater. *Environ Dev Sustain* 22(6):5873–5886
- Goel AK, Singh SN (2020b) Experimental study of heat transfer characteristics of an impinging jet solar air heater with fins. *Environ Dev Sustain* 22(4):3641–3653
- Goel AK, Singh SN, Prasad BN (2022) Experimental investigation of thermo-hydraulic efficiency and performance characteristics of an impinging jet-finned type solar air heater *Sustainable Energy Technol. Assess.* 52:B: 102165
- Goel AK, Singh SN (2021) Experimental performance evaluation of an impinging jet with fins type solar air heater. *Exp Sci Pollut Res* 28:19944–19957. <https://doi.org/10.1007/s11356-020-12193>
- Hassan AK, Hasan MM, Khan ME (2021) Parametric investigation and correlation development for heat transfer and friction factor in multiple arc dimple roughened solar air duct. *Renewable Energy* 174:403–425
- Heo E, Kim J, Boo KJ (2010) Analysis of the assessment factors for renewable energy dissemination program evaluation using fuzzy AHP. *Renew Sustain Energy Rev* 14(8):2214–2220
- Incropera FP, Lavine AS, DeWitt DP (2011) *Fundamentals of heat and mass transfer*. John Wiley & Sons Incorporated
- Ishizaka A, Labib A (2011) Review of the main developments in the analytic hierarchy process. *Expert Syst Appl* 38:14336–14345
- Jain PK, Lanjewar A, Rana KB, Meena ML (2021a) Effect of fabricated V-ribs roughness experimentally investigated in a rectangular channel of solar air heater: a comprehensive review 28: 4019–55 <https://doi.org/10.1007/s11356-020-11415-6>
- Jain PK, Lanjewar A, Jain R, Rana KB (2021b) Performance analysis of multi-gap V-roughness with staggered elements of solar air heater based on artificial neural network and experimental investigations 28: 32905–20 <https://doi.org/10.1007/s11356-021-12875-0>
- Kahraman C, Kaya I, Cebi S (2009) A comparative analysis for multiattribute selection among renewable energy alternatives using fuzzy axiomatic design and fuzzy analytic hierarchy process. *Energy* 34(10):1603–1616
- Kashyap A, Kumar R, Singh P, Goel V (2021) Solar air heater having multiple V-ribs with multiple-symmetric gaps as roughness elements on absorber-plate: a parametric study. *Sustain Energy Technol Assess* 48:101559
- Kline SJ, McClintock FA (1953) Describing uncertainties in single-sample experiments. *Mech Eng* 75:3–8
- Kumar D, Majanta P, Kalita P (2021) Performance analysis of a solar air heater modified with zig-zag shaped copper tubes using energy-exergy methodology. *Sustainable Energy Technol. Assess.* 46:101222. ()
- Landrigan PJ, Bernstein A, Binagwaho A (2020) COVID-19 and clear air: an opportunity for radical change. *Lancet Planet Health* 4(10):447–449
- Moffat RJ (1985) Using uncertainty analysis in the planning of an experiment. *J Fluids Eng* 107(2):173–178
- Perera F (2017) Pollution from fossil-fuel combustion is the leading environmental threat to global pediatric health and equity: Solutions exist. *Int. J. of Environ. Res. Public Health* 15:16
- Picard A, Davis RS, Glaser M, Fujii K (2008) A revised formula for the density of moist air (CIPM-2007). *Metrologia* 48:149–155
- Rahmani E, Moradi T, Fattahi A, Delpisheh M, Karimi N, Ommi F, Saboohi Z (2021) Numerical simulation of a solar air heater equipped with wavy and raccoon-shaped fins: The effect of fin's height. *Sustain Energy Technol Assess* 45:101227
- Rani P, Tripathy PP (2022) Heat transfer augmentation of flat plate solar collector through a finite element-based parametric study. *J Therm Anal Calorim* 147:639–660. <https://doi.org/10.1007/s10973-020-10208-w>
- Saaty TL (2008) Decision-making with the analytic hierarchy process. *Int J Services Sciences* 1(1):83–98
- Sahu MK, Matheswaran MM, Bishnoi P (2021) Experimental study of thermal performance and pressure drop on a solar air heater with different orientations of arc-shape rib roughness. *J Therm Anal Calorim* 144:1417–1434. <https://doi.org/10.1007/s10973-020-09569-z>
- Salman M, Chauhan R, Kim SC (2021a) Exergy analysis of solar heat collector with air-jet impingement on dimple-shape-roughened absorber surface. *Renewable Energy* 179:918–928
- Salman M, Park MH, Chauhan R, Kim SC (2021b) Experimental analysis of single loop heat collector with jet impingement over indented dimples. *Renewable Energy* 169:618–628
- Singh T, Patnaik A, Chauhan R (2016) Optimization of tribological properties of cement kiln dust-filled brake pad using grey relation analysis. *Mater Des* 89:1335–1342
- Sharma A, Chauhan R, Singh T, Kumar A, Kumar R, Kumar A, Sethi M (2017) Optimizing discrete V obstacle parameters using a novel Entropy-VIKOR approach in a solar air flow channel. *Renewable Energy* 106:310–320
- Skullong S, Promvong P, Thianpong C, Pimsarn M (2016) Thermal performance in solar air heater channel with combined

- wavy-groove and perforated-delta wing vortex generators. *Appl Therm Eng* 100:611–620
- Skullong S, Promvong P, Thianpong C, Jayranaiwar N, Pimsarn M (2017) Heat transfer augmentation in a solar air heater channel with combined winglets and wavy grooves on absorber plate. *Appl Therm Eng* 122:268–284
- Alam T, Meena CS, Balam NB, Kumar A, Cozzolino R (2021) Thermo-hydraulic performance characteristics and optimization of protrusion rib roughness in solar air heater. *Energies* 14(11):3159
- Wang YZ, Zhao J, Wang Y, An QS (2017) Multi-objective optimization and grey relational analysis on configurations of organic Rankine cycle. *Appl Therm Eng* 114:1355–1363
- Xu H, Sze JY, Romagnoli A, Py X (2017) Selection of Phase Change Material for Thermal Energy Storage in Solar Air Conditioning Systems. *Energy Procedia* 105:4281–4288
- Yu R, Han H, Yang C, Luo W (2021) Optimal design and decision making of an air cooling channel with hybrid ribs based on RSM and NSGA-II. *J Therm Anal Calorim*. 2021 <https://doi.org/10.1007/s10973-021-10807-1>
- Yu SM, Wang J, Wang JQ (2017) An interval Type-2 fuzzy likelihood-based MABAC approach and its application in selecting hotels on a tourism website. *Int J Fuzzy Syst* 19(1):47–61
- Zhao M, Wie G., Chen X, Wei Y (2021) Intuitionistic fuzzy MABAC method based on cumulative prospect theory for multiple attribute group decision making. *Int J Int Syst* 1–23
- Publisher's Note** Springer Nature remains neutral with regard to jurisdictional claims in published maps and institutional affiliations.
- Springer Nature or its licensor (e.g. a society or other partner) holds exclusive rights to this article under a publishing agreement with the author(s) or other rightsholder(s); author self-archiving of the accepted manuscript version of this article is solely governed by the terms of such publishing agreement and applicable law.